Lagrangian surface signatures reveal upper-ocean vertical displacement conduits near oceanic density fronts

H.M. Aravind [a], Vicky Verma [b], Sutanu Sarkar [b], Mara A. Freilich [c], Amala Mahadevan [d], Patrick J. Haley [e], Pierre F.J. Lermusiaux [e], Michael R. Allshouse [a,*]

[a] *Mechanical and Industrial Engineering, Northeastern University, Boston, 02115, MA, USA*
[b] *Mechanical and Aerospace Engineering, University of California San Diego, La Jolla, 92093, CA, USA*
[c] *MIT–WHOI Joint Program in Oceanography, Cambridge, 02139, MA, USA*
[d] *Woods Hole Oceanographic Institution, Woods Hole, 02543, MA, USA*
[e] *Department of Mechanical Engineering, Massachusetts Institute of Technology, Cambridge, 02139, MA, USA*

ARTICLE INFO

ABSTRACT

Vertical transport in the ocean plays a critical role in the exchange of freshwater, heat, nutrients, and other biogeochemical tracers. While there are situations where vertical fluxes are important, studying the vertical transport and displacement of material requires analysis over a finite interval of time. One such example is the subduction of fluid from the mixed layer into the pycnocline, which is known to occur near density fronts. Divergence has been used to estimate vertical velocities indicating that surface measurements, where observational data is most widely available, can be used to locate these vertical transport conduits. We evaluate the correlation between surface signatures derived from Eulerian (horizontal divergence, density gradient, and vertical velocity) and Lagrangian (dilation rate and finite time Lyapunov exponent) metrics and vertical displacement conduits. Two submesoscale resolving models of density fronts and a data-assimilative model of the western Mediterranean were analyzed. The Lagrangian surface signatures locate significantly more of the strongest displacement features and the difference in the expected displacements relative to Eulerian ones increases with the length of the time interval considered. Ensemble analysis of forecasts from the Mediterranean model demonstrates that the Lagrangian surface signatures can be used to identify regions of strongest downward vertical displacement even without knowledge of the true ocean state.

1. Introduction

Vertical transport in the upper ocean is instrumental in surface mixing, nutrient supply in the biogeochemical cycle (Denman and Gargett, 1995; Martin and Richards, 2001; Mahadevan, 2016), and the ocean energy budget (Wunsch and Ferrari, 2004; Gnanadesikan et al., 2005; Siegelman et al., 2020). It is also one of the mechanisms that govern the distribution of microplastics (Reisser et al., 2015) and other chemical pollutants (Tanabe and Tatsukawa, 1983; González-Gaya et al., 2019) in the ocean. Observational investigation of vertical transport, however, is considerably more difficult than studying horizontal transport because vertical velocities in the ocean $\left(O\left(10^{-4} \text{ m s}^{-1}\right)\right)$ are orders of magnitude smaller than the horizontal components $\left(O\left(0.1^{-4} \text{ m s}^{-1}\right)\right)$ (Mahadevan, 2016; Mahadevan et al., 2020b). Additionally, the vertical velocity magnitudes are near the noise-limit for most acoustic Doppler current profilers (Fischer and Visbeck, 1993), making direct measurements difficult. The combined impact of waves, eddies, and wind-driven Ekman dynamics result in a highly variable vertical velocity field where the influence of any one phenomenon is hard to distinguish.

One quantity of interest when studying vertical transport is the time-integrated vertical displacement (i.e. change in depth) of fluid-particle trajectories over a time interval of hours to days. These measurements of vertical displacements are on the order of tens to hundreds of meters over fluid-particle trajectories that extend kilometers in the horizontal direction. Even when downward displacement of fluid is observed in the ocean, only a fraction undergoes "subduction", which is the transfer of fluid from the surface mixed layer into the pycnocline and stratified interior (Spall, 1995; Marshall, 1997; Williams and Meijers, 2019; Mahadevan et al., 2020b). Oceanographers have proposed the existence of three-dimensional coherent pathways at sites of subduction that act as conduits for exchange from the surface to the interior (Mahadevan et al., 2020a,b). For short time intervals, particles inside vertical transport conduits initially near the surface can undergo downward displacement but remain in the mixed layer while those that start

deeper may undergo subduction by leaving the mixed layer. Recent studies have shown that these sites are closely linked to submesoscale ($O(1\,\text{km})$ horizontal length scale) features (McWilliams, 2016) such as density fronts, and are not randomly distributed (Ruiz et al., 2019).

Numerical studies based on high resolution ocean models demonstrate how submesoscale dynamics near oceanic density fronts dominate vertical transport in the ocean and that Ekman pumping resulting from wind forcing on the surface is insufficient to fully account for the observed vertical transport signatures (Mahadevan and Tandon, 2006; Giordani et al., 2006; Thomas et al., 2008; Nagai et al., 2015). Field studies guided by insights from numerical studies of submesoscale eddies (Omand et al., 2015) and oceanic density fronts (Pascual et al., 2017; Mahadevan et al., 2020b) have confirmed the importance of submesoscale processes in dictating ocean vertical transport. More recent numerical studies have suggested the existence of filaments of concentrated vorticity that are $O(0.1\,\text{km})$ wide along the perimeter of submesoscale eddies that serve as coherent pathways for vertical motions in the ocean (Mahadevan, 2006; Omand et al., 2015; Freilich and Mahadevan, 2019; Verma and Sarkar, 2021). Although numerical simulations using ocean models can provide insight into vertical transport mechanisms by generating three-dimensional velocity fields, a combination of ocean modeling and observational field experiments (Lermusiaux et al., 2006b) is required to understand and verify the various mechanisms that result in enhanced vertical velocities and the underlying pathways (Omand et al., 2015; D'Asaro et al., 2018) of vertical transport. Experimental investigations of these coherent pathways require precise targeting of the conduits that may be located along submesoscale vorticity filaments near oceanic density fronts.

In order to locate vertical transport conduits during an observational study, the method should rely on ocean surface signatures where measurements are most prevalent. To identify regions near the ocean surface where strong vertical transport is anticipated, surface fields from ocean forecasts and satellite altimetry are used (Mahadevan et al., 2020b). Ideally, a vertical velocity field could be used to locate regions of strong instantaneous downwelling, but reliable estimates are hard to obtain due to being orders of magnitude smaller than the horizontal components. Alternatively, computation of the negative horizontal divergence of the surface horizontal velocity field can highlight regions of instantaneous surface convergence, which correspond to downwelling at that instant. During field experiments, the divergence can be estimated using trajectories of drifter swarms (Molinari and Kirwan, 1975; Berta et al., 2016; D'Asaro et al., 2018; Berta et al., 2020; Tarry et al., 2021). Recent numerical and observational studies have investigated the link between divergence and enhanced vertical motion near oceanic density fronts (Barkan et al., 2019). The instantaneous location of these fronts, which are known to feature enhanced vertical velocities, can be identified using the horizontal density gradient on the surface. While some of these Eulerian metrics are measurable during field experiments, they are only capable of revealing the instantaneous state of the ocean like an instantaneous "subduction rate", which is often defined as the flux of fluid through a depth surface (Marshall et al., 1993; Qu and Chen, 2009). Hence, their ability to predict vertical displacement, an intrinsically Lagrangian phenomenon that occurs over a finite time interval, may be limited.

A Lagrangian analysis is more indicative of cumulative vertical transport, but the predictive value of a Lagrangian analysis of real-time data to identify sites of deeper displacement beyond the time interval of analysis is unknown. Moreover, individual trajectories computed from model forecasts are highly sensitive to noise and model error, so it may not provide robust prediction of where vertical transport may occur in the real ocean. Lagrangian metrics such as the finite-time Lyapunov exponent (FTLE) (Haller, 2001) and dilation rate (Huntley et al., 2015), which are robust to noise (Haller, 2002), can be used to identify regions of surface convergence. These metrics have been widely employed in the calculation of Lagrangian coherent structures (Allshouse and Peacock, 2015; Haller, 2015) to identify transport barriers in fluid flows. Two-dimensional coherent structure calculations have been used to identify two-dimensional transport features (Olascoaga et al., 2006; d'Ovidio et al., 2009; Hernández-Carrasco et al., 2018) and link them to surface circulation and local mixing (Choi et al., 2017). These structures and their three-dimensional extensions, however, have yet to be used to target vertical transport through coherent conduits in the upper ocean. Performing a three dimensional coherent structure analysis may potentially reveal the structure of these conduits, but it is not feasible due to the lack of accurate three dimensional oceanic fields. Furthermore, leveraging the available drifter data requires performing an analysis that restricts trajectory advection to the two dimensional surface. In a general three dimensional system, the analysis of a two dimensional slice of the domain provides useful information about the full three dimensional transport only in unique conditions (Sulman et al., 2013). Fortunately, in an oceanic setting, where large scale motions are predominantly horizontal, it is reasonable to consider the two-dimensional surface signatures as representative of the weakly three dimensional processes in the upper ocean. In fact, field experiments that investigate subduction in the ocean look for some surface signatures, like convergence of drifter trajectories (D'Asaro et al., 2018; Mahadevan et al., 2020b).

Because the available measurements are drawn from the ocean surface, the influence of these surface converging zones will be most relevant for vertical displacements and subduction of particles that are initially near the surface. Two challenges with this initial placement are that these particles will be exposed to the weak vertical velocities near the surface and will have to be transported through the entire mixed layer to subduct into the ocean interior. As a result, some of the vertical displacement observed may not necessarily mean that a particular particle has undergone subduction. However, the particles in the strongest vertical displacement conduits can potentially leave the mixed layer if a longer time interval is considered or if they are initialized deeper in the water column. Hence, our analysis focuses on linking the surface Lagrangian and Eulerian metrics to regions of significant vertical displacement.

To test the ability of Lagrangian and Eulerian surface metrics to locate regions of strong downward displacement of fluid, we analyze the method applied to three ocean models ranging in scale from kilometers to hundreds of kilometers. The smallest model considered is a large eddy simulation model that captures the detailed dynamics of density front filamentation and how the turbulence impacts the local transport (Verma et al., 2019). Next, a process study ocean model considers the evolution of a zonally oriented density front and its interaction with submesoscale eddies and vorticity filaments, with initial conditions constructed using observed temperature and salinity measurements in the Mediterranean (Mahadevan et al., 1996a,b; Freilich and Mahadevan, 2019, 2021; Dever et al., 2020). Finally, a data-assimilative real-time operational model of the Mediterranean that comprises multiple density fronts that co-exist with other flow features like basin-wide gyres is considered, which provides the most realistic setting for field experiments (Haley and Lermusiaux, 2010; Haley et al., 2015; Mahadevan et al., 2020a). Each of these models features a density front, contains submesoscale features and utilizes markedly different underlying assumptions. The analyses of Verma and Sarkar (2021) and Freilich and Mahadevan (2021) have presented evidence of coherent downward transport in the turbulence resolving and process study models and, additionally, Freilich and Mahadevan (2021) find subduction to below the mixed layer. By applying our method to these models of different scale and physics, we are able to evaluate the robustness of applicability of Lagrangian and Eulerian metrics.

In this paper, we propose the use of two Lagrangian metrics computed using surface horizontal velocities to predict regions of high sub-surface downward displacement of fluid in the ocean. The regions where these metrics are strongest are considered target zones for downward displacement, and the efficacy of these target zones in locating large vertical displacements is evaluated using skill metrics that quantify how likely they are to predict regions of large displacements and

the fraction of such regions identified by the target zones. The correspondence between the surface target zones and sub-surface δz fields computed for particles initialized at different depths below the surface is then studied to evaluate the range of applicability of the target zones. A practical concern when performing a Lagrangian analysis is the time interval of applicability of results. Hence, we investigate the effect of varying the time interval of Lagrangian analysis, and the ability of the chosen Lagrangian metrics to predict large displacements occurring beyond that interval. Finally, since model forecasts do not capture the true state of the ocean (McWilliams, 2007), the ability of target zones identified across an ensemble of forecasts to locate regions of strong downward displacement in a separate realization is evaluated with a data-assimilative operational model of the western Mediterranean.

2. Methods

2.1. Vertical displacement, surface metrics and target zones

Conduits of vertical transport can be located by identifying regions with fluid trajectories that show large vertical displacements. Given a velocity field $\mathbf{u} = (u, v, w)$ specified at $\mathbf{x} = (x, y, z)$, fluid trajectories are solutions to

$$\frac{\mathrm{d}\mathbf{x}}{\mathrm{d}t} = \mathbf{u}(\mathbf{x}, t). \tag{1}$$

For each of the three models, particles are seeded uniformly on a horizontal plane at $z(t = t_0)$ below the surface and then advected by solving Eq. (1) using a fourth order Runge–Kutta scheme. Velocities for particle advection are obtained from model fields using a cubic Lagrange polynomial for temporal interpolation, followed by a bilinear interpolation in space. The downward vertical displacement (δz) undergone by particles seeded at depth $z(t = t_0)$ is then computed as

$$\delta z = z(t_0) - z(t_0 + T_d), \tag{2}$$

where the displacement time T_d is the time over which advection is performed. In our study, a 12 h interval has been used for the two larger-scale models, whereas a smaller $T_d = 6$ h is used for the turbulence resolving model so that the non-dimensional value $T_d/(2\pi/f)$ remains approximately 0.5 across the three models.

Next, we compute Eulerian and Lagrangian metrics that can potentially identify regions of high δz using only surface information. The most intuitive measure of vertical motions, given a velocity field, is the vertical velocity w. Because $w < 0$ corresponds to downwelling, the negative vertical velocity ($-w$) at time t_0 is the first metric. It is important to note that although w highlights regions of strongest vertical motion at an instant, the Eulerian field need not be representative of vertical displacement that occurs over a finite time interval. Another drawback of this metric is that vertical velocities are often difficult to measure in the ocean and model accurately. The horizontal velocities, on the other hand, are measurable, and incompressibility dictates that convergence on the ocean surface corresponds to downwelling. Therefore, the negative horizontal divergence of surface velocity ($-\nabla_H \cdot \mathbf{u}$), positive for downwelling, is the second Eulerian metric. Physically, surface convergence is enhanced at submesoscale density fronts in the ocean, which are known to be sites of intense vertical motions (Mahadevan and Tandon, 2006). Hence, the magnitude of the horizontal gradient of surface density ($|\nabla_H \rho|$), which can be measured observationally (Pascual et al., 2017; Rudnick and Klinke, 2007; Ullman and Hebert, 2014), is the final Eulerian metric. All of these Eulerian metrics are computed only at the initial instant, t_0. The inability to obtain accurate measurements of w prompts the usage of the other Eulerian metrics for practical purposes. In this study, however, the Eulerian metric w is available from the models and is used as a barometer to compare the other metrics with. In all three models considered, w is computed on the horizontal layer just below the ocean surface. This can impact our results, especially in the process study model, as will be discussed later.

To better account for the Lagrangian nature of vertical displacement, two Lagrangian metrics are computed on the ocean surface: FTLE and dilation rate. Solving Eq. (1) for x and y at $z = 0$, using only the horizontal velocity and setting $w = 0$, allows us to define the two-dimensional flow map, $F_{t_0}^{t_0+T_L}(\mathbf{x}_0) := \mathbf{x}(t_0 + T_L; \mathbf{x}_0, t_0)$, that maps particles seeded at $\mathbf{x}_0 = (x_0, y_0, 0)$ at time t_0 to their final positions at $t_0 + T_L$. Here, T_L is the length of the time interval over which the Lagrangian metrics are calculated, and this may or may not be the same as the displacement time, T_d, depending on the time over which accurate surface velocity fields are available. The flow map gradient, $\nabla F_{t_0}^{t_0+T_L}(\mathbf{x}_0)$, is then used to compute the right Cauchy–Green strain tensor $C = [\nabla F_{t_0}^{t_0+T_L}(\mathbf{x}_0)]^\top [\nabla F_{t_0}^{t_0+T_L}(\mathbf{x}_0)]$. Given the two eigenvalues of C, $0 < \lambda_1 < \lambda_2$, the FTLE ($\sigma$) at time t_0 is

$$\sigma = \frac{\log \lambda_2}{2 T_L}, \tag{3}$$

and the dilation rate (Δ) at t_0 is

$$\Delta = \frac{\log \lambda_1 \lambda_2}{2 T_L}. \tag{4}$$

The dilation rate is the Lagrangian time-average of the Eulerian divergence ($\nabla_H \cdot \mathbf{u}$) along the trajectory (Huntley et al., 2015). It is worth noting that the Lagrangian metrics computed along particle trajectories differ from metrics obtained by averaging at a fixed location in space. Another potential metric that could be considered is the instantaneous Lyapunov exponent (iLE) (Nolan et al., 2020), which is the Eulerian infinitesimal time limit of FTLE. This metric has been employed for the detection of objective Eulerian coherent structures (Serra and Haller, 2016), but its ability to locate regions of strong δz is similar to the other Eulerian metrics (Figure S1, Supporting Information).

When the Lagrangian metrics are computed forward in time from t_0 to $t_0 + T_L$, the two-dimensional FTLE and dilation rate fields obtained at the initial time t_0 physically represent the amount of maximal directional expansion and area expansion rates over the time interval, respectively. Since we are interested in surface convergence instead of expansion, these quantities need to be computed starting at the end of the time interval $t_0 + T_L$ and moving backwards in time to the beginning of the interval t_0 (Haller, 2015). A backward-in-time calculation, however, yields Lagrangian fields at $t_0 + T_L$, which do not correspond to the δz field at t_0. To make the direct comparison possible, we map the Lagrangian metric fields to their position at t_0. Additionally, result independence from interpolation and advection parameters was ensured for all numerically extracted particle trajectories, and hence the results are comparable to those from online calculations performed during model runs (Van Sebille et al., 2018).

The five metrics discussed above are chosen such that the regions with the largest values of these metrics should correspond to regions of greatest downwelling. Hence, the target zone (TZ) for each metric is defined as the region with values in the 99th percentile of the respective Eulerian or Lagrangian metric computed on the ocean surface. As a result, each target zone covers only 1% of the entire domain. The choice of 1% is based on our study varying the threshold (presented in Figure S2, Supporting Information), such that the TZs identify only the strongest δz regions, while being large enough to yield regions that are not trivially small. The choice of the target threshold need not be universal; however, in the cases studied here, 1% was found to be ideal. The TZs can also be used to predict regions of strongest δz when computed using model forecasts, as discussed later. To quantify the ability of each metric's TZ to identify regions of strong downward vertical displacement, we investigate the extent of overlap between the TZ derived from the metric on the ocean surface and the regions of strongest δz below the surface.

2.2. Numerical models analyzed

Three different ocean models are analyzed to evaluate the robustness of the target zones capacity to identify sites of strongest downward
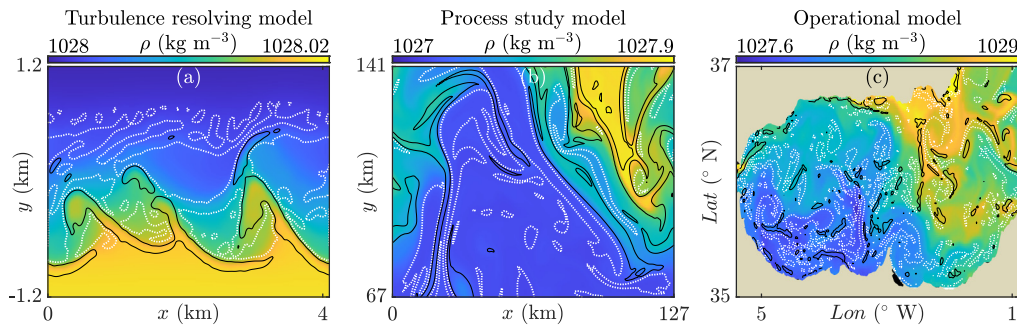
Fig. 1. Models analyzed. Surface density fields at the initial time ($t = t_0$) for (a) the turbulence resolving model of a front, (b) process study model of a front and (c) operational model of the western Mediterranean. Density fields are plotted in color, and the gradients indicate locations of density fronts. Contours of the vertical vorticity non-dimensionalized by the planetary vorticity (ω_z/f), which is indicative of the local Rossby number, are overlaid. The negative contours (anti-cyclonic vorticity, dashed white) correspond to ω_z/f values of (a) -0.5, (b) -0.5 and (c) -0.4, and the positive contours (cyclonic vorticity, solid black) to (a) 1, (b) 0.5 and (c) 0.8. The domains analyzed in (a) and (b) focus on the density front and do not span the entire numerical domain.

vertical displacement. Given the connection between submesoscale features and subduction, we consider three models that each produce submesoscale features by accounting for different flow physics at spatial scales spanning two orders of magnitude. Fig. 1 presents the surface density field at t_0, the time at which we start our analysis. The horizontal gradient in the density field highlights the location and structure of the density front in each system. Contours of the non-dimensional vertical vorticity are plotted to highlight the regions of submesoscale fronts and eddies, which are related to regions of subduction (Mahadevan and Tandon, 2006).

The first model analyzed is a large eddy simulation of an oceanic density front under the influence of rotation by solving the non-hydrostatic Navier–Stokes equations under the Boussinesq approximation (Verma et al., 2019). The domain for the turbulence resolving simulation spanned $4\,\text{km} \times 6\,\text{km}$ in the horizontal, was 130 m deep, and had a resolution of 2 m in all directions. The initial three-dimensional temperature profile features a 1.2 km wide east–west density front confined in a surface layer with depth 50 m. The initial velocity profile is obtained by integrating the density field to satisfy the thermal wind balance. The specified set of initial conditions establishes a density front which is geostrophically balanced by a surface jet along the front. Periodic boundary conditions are used along the front, and free-slip (velocity) and no-flux (temperature) conditions are used on the surface and cross-front boundaries. A constant heat flux and free-slip condition for velocity are used on the bottom boundary.

This high resolution model captures the impact that turbulence has on the submesoscale eddies and the resulting vertical transport. Since only submesoscale fluid motions play the dominant role in sustained downward transport (Verma and Sarkar, 2021) and the turbulence introduced features at length scales below the features we are interested in, we present our analysis on filtered submesoscale fields that remove the fine-scale turbulent fluctuations from the model output without removing the larger scale impact of modeling turbulence. Corresponding analysis of the unfiltered fields over a shorter displacement time is presented in Figure S3 (Supporting Information) and yields qualitatively similar results to the filtered data. The gradient in the submesoscale density field and the vorticity contours at t_0 (Fig. 1a) reveal a density front deformed by baroclinic instability, resulting in the formation of submesoscale eddies and vorticity filaments along the front. Modeled submesoscale vertical velocities are as large as $3.5 \times 10^{-3}\,\text{m s}^{-1}$ near the vorticity filaments and the periphery of the submesoscale vortices, where downward displacement of up to $\delta z_{max} = \sim 35\,\text{m}$ is observed over 6 h. This corresponds to a vertical displacement rate of $\delta z_{max}/T_d = 1.6 \times 10^{-3}\,\text{m s}^{-1}$, which is an order of magnitude larger than vertical velocities observed in large-scale numerical models of the ocean. The displacement time of $T_d = 6\,\text{h}$ corresponds to a non-dimensional value $T_d/(2\pi/f) = 0.48$, where $f = 1.4 \times 10^{-4}\,\text{s}^{-1}$ is the Coriolis parameter for the model. The model outputs

were saved approximately every 400 s, and three-dimensional particle advection was performed over $T_d = 6\,\text{h}$ using a time-step of 60 s. To obtain converged two-dimensional trajectories over $T_L = T_d = 6\,\text{h}$ for computing the Lagrangian metrics using the horizontally divergent two-dimensional surface velocity field, however, a smaller time-step of 10 s was required. Due to the strong convergence on the surface, analysis of two-dimensional trajectories computed over time intervals of 12 h or more revealed non-negligible accumulation of numerical error even for smaller time-steps at the strongest converging regions. Hence, we use a non-dimensional time of $T_d/(2\pi/f) \approx 0.5$ (which corresponds to $T_d = 6\,\text{h}$ for the turbulence resolving model) for all three models analyzed.

Next, we analyze the process study ocean model (Mahadevan et al., 1996a,b; Freilich and Mahadevan, 2019, 2021; Dever et al., 2020) initialized with a geostrophically balanced front oriented zonally in a periodic channel. The model solves the non-hydrostatic Navier–Stokes equations in a $128\,\text{km} \times 206\,\text{km} \times 1\,\text{km}$ domain, at a horizontal resolution of $\sim$500 m. The domain has periodic boundary conditions in the east–west direction and free-slip conditions at the bottom, north, and south boundaries. The initial temperature and salinity is constructed using observed Western Mediterranean thermocline structure with 50 m–70 m mixed layer, and the model is cooled uniformly. The temperature gradient on the surface results in an initial density front that runs in the east–west direction, and the initial flow is in thermal wind balance, without any wind forcing on the surface. Subgridscale mixing is parameterized with a $1\,\text{m}^2\,\text{s}^{-1}$ horizontal diffusivity and $1 \times 10^{-4}\,\text{m}^2\,\text{s}^{-1}$ vertical diffusivity.

Owing to its spatial resolution of 500 m, the model does not capture the sub-kilometer-scale turbulence observed in the previous model, but it does simulate the baroclinic instability with submesoscale physics. The density field at t_0 (Fig. 1b) presents the evolved structure of the density front. Contours of non-dimensional vorticity indicate the location of submesoscale eddies and vorticity filaments, which are observed on either side of the front. The strongest vertical velocities observed in this model ($1.4 \times 10^{-4}\,\text{m}^{-2}\,\text{s}^{-1}$) are smaller than the turbulence resolving model, and hence, particles seeded near the surface are not displaced more than 8 m downward over $T_d = 12\,\text{h}$ — here, $T_d/(2\pi/f) = 0.47$, where the Coriolis parameter $f = 0.7 \times 10^{-4}\,\text{s}^{-1}$. The vertical velocities in this model are smaller than the turbulence resolving model due to the large horizontal diffusivity, and the boundary layer turbulence parameterization. Both the two-dimensional and three-dimensional particle trajectory advection for this model were performed from the 3-hourly model output using a time-step of 60 s to obtain converged trajectories.

The third model considered is a data-assimilative real-time operational model of the western Mediterranean (Haley and Lermusiaux, 2010; Haley et al., 2015; Mahadevan et al., 2020a). The simulations were performed using the MIT Multidisciplinary Simulation, Estimation and Assimilation Systems (MIT-MSEAS) primitive equation ocean
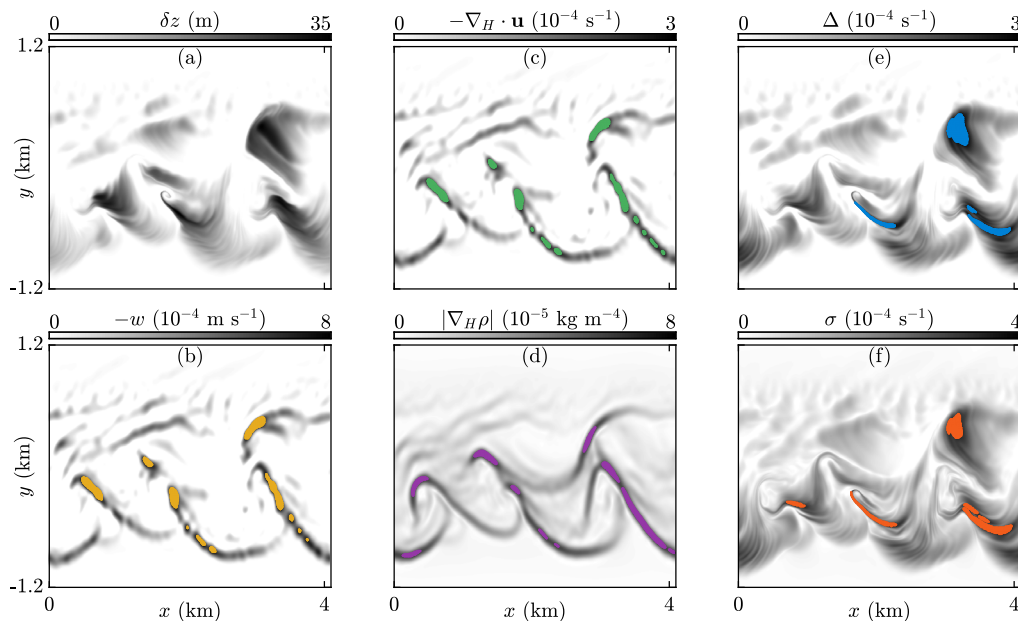
Fig. 2. Downward vertical displacement below the surface, surface metrics and corresponding target zones for the turbulence resolving model of a density front. (a) The δz field for particles released at a depth of $4\,\mathrm{m}$, computed over the interval $[t_0, t_0 + T_d]$ and plotted at t_0. Eulerian surface target zones at t_0: (b) negative vertical velocity ($-w$), (c) negative horizontal divergence of velocity ($-\nabla_H \cdot \mathbf{u}$), and (d) horizontal density gradient magnitude ($|\nabla_H \rho|$). Lagrangian surface target zones, computed over the interval $[t_0, t_0 + T_L]$ and plotted at t_0: (e) dilation rate (Δ) and (f) FTLE (σ). The target zones for each metric are overlaid in color in panels (b)–(f). Note that, for the turbulence resolving model, $T_d = T_L = 6\,\mathrm{h}$.

modeling system (Haley and Lermusiaux, 2010; Haley et al., 2015). The computational domain spanned approximately $430\,\mathrm{km} \times 267\,\mathrm{km}$ in the horizontal at a resolution of $\sim 500\,\mathrm{m}$, with 70 optimized terrain-following vertical levels based on the SRTM15+ bathymetry (Tozer et al., 2019). Surface forcing for the simulations was based on the atmospheric fluxes from the $1/4°$ NCEP Global Forecast System product and tidal forcing from the high-resolution TPX08-atlas (Egbert and Erofeeva, 2002). Initial conditions were obtained from three different models: $1/12°$ Hybrid Coordinate Ocean Model, $1/24°$ Copernicus Marine Environment Monitoring Service, and $\sim 1/50°$ Western Mediterranean Operational forecasting system. These were corrected using observational data from Argo floats and, whenever possible, moorings. The downscaled forecasts of the western Mediterranean were used as central forecasts for the ensemble forecasting method using the Error Subspace Statistical Estimation schemes (Lermusiaux, 2002). The initial 3D perturbations were constructed from a combination of vertical empirical orthogonal functions of historical March CTD data along with an eigendecomposition of a horizontal correlation matrix computed using a 12.5 km decay scale and a 31.25 km zero-crossing. A 3D primitive equation balance was applied to the perturbed velocities.

The dense, salty water in the Mediterranean meets a jet of lighter water from the Atlantic entering through the Strait of Gibraltar, resulting in the formation of strong density fronts and coherent basin-scale gyres. The gradient in the density field in Fig. 1c identifies the location of these fronts on 12 Apr 2019 12:00:00, and the contours of non-dimensional vorticity roughly align with the location of the mesoscale gyres. The gyres are not stationary, nor are they constantly present (Heburn and La Violette, 1990; Vargas-Yáñez et al., 2002; Pascual et al., 2017). A reference value of the Coriolis parameter for this region is $f = 0.86 \times 10^{-4}\,\mathrm{s}^{-1}$. Vertical velocities of up to $\sim 5 \times 10^{-3}\,\mathrm{m}\,\mathrm{s}^{-1}$ are observed near the surface, and downward displacement of up to $\delta z_{max} = 130\,\mathrm{m}$ is observed over $T_d = 12\,\mathrm{h}$, which corresponds to a non-dimensional displacement time of $T_d/(2\pi/f) = 0.59$. The corresponding vertical displacement rate ($\delta z_{max}/T_d = 3 \times 10^{-3}\,\mathrm{m}\,\mathrm{s}^{-1}$) is indicative of regions of strong vertical transport in the Mediterranean, owing to intense vertical motions near the fronts. Converged particle trajectories in the operational model were computed from 3-hourly model outputs using a time-step of $60\,\mathrm{s}$.

3. Results

We begin by analyzing the turbulence resolving model, which provides the highest fidelity model of the dynamics near a density front. The δz field, the five surface metrics and their corresponding target zones, computed for the turbulence resolving model, are presented in Section 3.1. The efficacy of TZs to identify regions of strongest downward vertical displacement is then quantified using various skill metrics for each of the models in Section 3.2. To understand the vertical length scale over which our results may be valid in a realistic setting, the effect of varying the seeding depth for δz measurements is investigated for the operational model in Section 3.3. Then practical concerns of the impact of time intervals and analyzing ensemble simulations are investigated in Sections 3.4 and 3.5, respectively.

3.1. Analysis of the turbulence resolving model

In this section, we discuss in detail the δz field, the five surface metrics and their corresponding target zones computed for the turbulence resolving model of a density front. The δz field for particles released at $z(t_0) = -4\,\mathrm{m}$ is calculated over a displacement time $T_d = 6\,\mathrm{h}$ and is presented in Fig. 2a. A seeding depth of $z_0 = -z(t_0) = 4\,\mathrm{m}$ was chosen to measure the downward vertical displacement of fluid initially close to, but below, the surface of the ocean. Based on Fig. 2a, four regions of strong δz are observed in the system. Figure S4 (Supporting Information) demonstrates that the δz fields are qualitatively similar down to a depth of $20\,\mathrm{m}$.

High-δz regions in the upper ocean remain nearly depth independent for all three models despite spanning various length scales (Table S1, Supporting Information) and this vertical correlation further justifies a search for surface TZs to locate vertical transport conduits. The instantaneous Eulerian metrics calculated on or just below the ocean surface at time t_0 are presented in Fig. 2b–d. Regions with the largest magnitudes of these metrics are concentrated near the vorticity filaments (as seen in Fig. 1a) and form sharper structures compared to δz in Fig. 2a. This is due to the Eulerian TZs highlighting the most dynamic regions on the surface at the instant t_0. In contrast, the δz field is computed over a finite time interval, which allows more of the
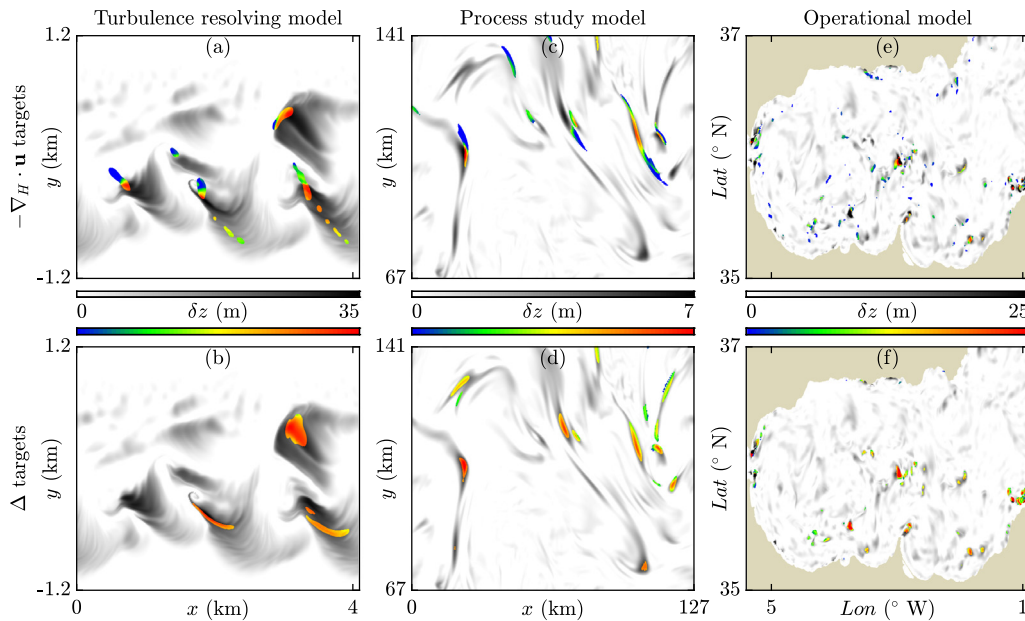
Fig. 3. Target zones overlaid on δz fields for the three models. The negative horizontal divergence $(-\nabla_H \cdot \mathbf{u})$ target zones (top) and dilation rate (Δ) target zones (bottom) overlaid (color) on δz fields (grayscale) calculated for the turbulence resolving model (a) and (b), the process study model (c) and (d), and the operational model of the western Mediterranean (e) and (f). Target zone overlays are plotted using a color map representing the δz value underneath. Shades of blue represent regions where the target zones do not correspond to strong downward displacement and the red regions represent target zones that have identified regions of strongest downward displacement.

fluid to collect towards and downwell along the transport pathways, ultimately resulting in broader regions of high δz. The dilation rate and FTLE fields computed on the surface for $T_L = T_d = 6\,\text{h}$ are presented in Fig. 2e,f. These Lagrangian fields computed over a time interval have broader features that are more representative of the δz field.

The TZs for each metric are overlaid over the respective fields in Fig. 2b–f. A comparison between the TZs of a metric and the high-δz regions provides an indication of the ability of the metric computed on the ocean surface to identify regions of strongest sub-surface vertical displacement. The Eulerian TZs observed in Fig. 2b–d are restricted to the filamentary regions, whereas the Lagrangian TZs in Fig. 2e,f are more reflective of the high-δz regions in Fig. 2a. This suggests that the Lagrangian TZs are better at identifying regions of stronger vertical displacement than the Eulerian ones.

3.2. Locating vertical displacement conduits in three submesoscale-resolving models

In order to evaluate if the benefit of using Lagrangian TZs over Eulerian is robust, we repeat the analysis over longer displacement times on different types of simulations that resolve physical processes at different scales. As was done for the turbulence resolving model, the δz field was computed for particles seeded at $4\,\text{m}$ for the process study and operational models. The displacement times for the larger scale models were $T_d = 12\,\text{h}$, a time scale that is relevant for physiological responses of biological populations that often operate on diel cycles (Dusenberry et al., 1999). As was the case for the turbulence resolving model, the Lagrangian TZs were computed for time intervals matching the displacement times (i.e., $T_L = T_d$).

Fig. 3 presents the target zones obtained from the Eulerian divergence metric and Lagrangian dilation rate metric for each model overlaid on the respective δz fields. Dilation rate is the chosen Lagrangian metric since it is the best metric considered for identifying high δz regions. Divergence is chosen as the Eulerian metric as opposed to vertical velocity based on practical considerations, and the fact that dilation rate is the Lagrangian average of divergence along a particle trajectory. The color of the TZ reflects the amount of underlying downward vertical displacement with red regions corresponding to where the TZ aligns with the high δz and the blue regions to low

δz. For the turbulence resolving model, the Eulerian TZs presented in Fig. 3a fail to align with a significant portion of regions of high δz. The Eulerian TZs also correspond to regions with hardly any downward vertical displacement as seen by the dark blue regions in Fig. 3a. The Lagrangian TZs, as seen from the preponderance of the red shades in Fig. 3b, better capture regions of high δz for $T_L = 6\,\text{h}$ for the turbulence resolving model. The difference in performance between the two TZs are more pronounced in the process study model (Fig. 3c,d) for which $T_L = 12\,\text{h}$ is a longer time interval. The Eulerian TZs rarely correspond to high-δz regions, whereas the Lagrangian TZs capture all regions of strongest downward vertical displacement. Qualitatively similar results are obtained for the operational model as well, with the divergence TZs failing to capture many regions of high δz (Fig. 3e), which are identified by the Lagrangian TZs (Fig. 3f). Similar overlays for the other three metrics are presented in Figure S5 (Supporting Information), wherein we observe that the Lagrangian FTLE TZs, which are similar to the dilation rate results, also outperform the Eulerian TZs.

To better quantify the degree of overlap between TZs and high-δz regions in Fig. 3 and Figure S5 (Supporting Information), skill metrics are computed and presented in Fig. 4. The probability distribution functions (PDFs) of δz corresponding to the metric target zones $f(\delta z|\text{Target})$ are presented in Fig. 4a,d,g. This corresponds to the probability that a particle seeded below the surface TZ will be displaced downward by δz. Fig. 4b,e,h present the corresponding complementary cumulative distribution functions (complementary CDFs) $\bar{F}(\delta z|\text{Target})$, which indicate the probability of a particle seeded below the TZ displacing downward by at least δz. While evaluating the extent of downward vertical displacement corresponding to the TZs is helpful, we are also interested in the fraction of the strongest δz zones that are identified by the TZs. The "target efficiency" indicates the fraction of regions corresponding to a downward vertical displacement of δz that are identified by a TZ, and is the third skill metric presented in Fig. 4c,f,i. The last two skill metrics, complementary CDF and target efficiency, can also be defined in terms of true positives (TP) or hits, false negatives (FN) or misses, and false positives (FP) or false alarms. The complementary CDF is equivalent to $TP/(TP+FP)$ and the target efficiency is $TP/(TP+FN)$. Fig. 4 also presents reference curves for the entire domain (no metric case), which corresponds to blindly sampling the domain, in black. Note that the third skill metric, the target efficiency, in Fig. 4c,f,i will always be
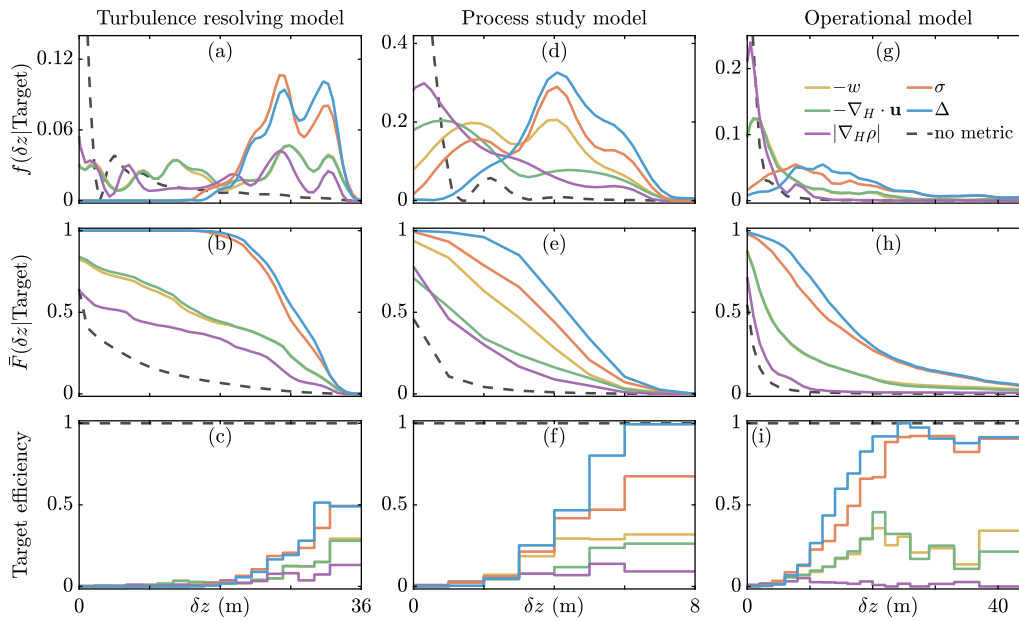
Fig. 4. Skill metrics of the Eulerian and Lagrangian target zones. Probability density functions (PDFs) of δz for each target zone $f(\delta z|\text{Target})$ (top), corresponding complementary cumulative distribution functions $\bar{F}(\delta z|\text{Target})$ (middle), and the target efficiency (bottom), plotted as a function of δz, for the turbulence resolving model (left), process study model (center) and operational model of the western Mediterranean (right). Legend for the metrics is presented in (g). Uniform bin-widths were chosen for the computation of the target efficiency, except for the bin corresponding to the largest δz values, which has a lower bin-count. Skill curves for the no-metric case are also plotted as black dashed lines for reference, to highlight the benefit of using Eulerian and Lagrangian target zones as opposed to blindly sampling the entire domain.

1 in this case since all regions with $\delta z > 0$ are already included in the target zone (entire domain).

For the turbulence resolving model, the PDFs for the Lagrangian TZs in Fig. 4a are skewed towards larger values of δz, compared to a more uniform distribution for the Eulerian TZs. This is in stark contrast to the PDF for the no metric case which is skewed towards $\delta z = 0$, indicating that on average there is no downwelling or upwelling in the domain. The median δz for the Lagrangian TZs (~ 27 m) is approximately double that of the Eulerian divergence and vertical velocity TZs (~ 15 m) and the density gradient TZs performed the worst with a median of only 6 m. The benefit of at least using an Eulerian metric is not to be dismissed, however, since the median δz for the divergence TZs is 14 m more than the value for the no metric case (less than 1 m), which is of the same order of magnitude as the gain when using the Lagrangian dilation rate TZs compared to divergence TZs. The Lagrangian TZs rarely identify regions of low δz, as indicated by $f(\delta z|\text{Target}) = 0$ for $\delta z < 15$ m. The PDFs for Eulerian TZs have non-zero values for $\delta z = 0$, indicating that a small fraction of these target zones result in no downwelling or small amounts of upwelling. This is not surprising since density fronts are sites of strong downwelling as well as upwelling (Verma et al., 2019). The complementary CDFs presented in Fig. 4b demonstrate that the Lagrangian TZs have a consistently higher probability of predicting any amount of downward vertical displacement δz, with the dilation rate marginally outperforming the FTLE. For example, Lagrangian TZs identify $\delta z > 20$ m more than 90% of the time, as opposed to 37% for the Eulerian TZs, even though δz of this magnitude occurs in only 5% of the domain. Furthermore, as observed in Fig. 4c, Lagrangian TZs identify approximately 50% of the strongest δz regions, despite targeting only 1% of the domain. Across all three skill metrics, there is clear benefit of using the Lagrangian TZs over the Eulerian TZs. Another interesting observation is that while the horizontal density gradient reveals the location of oceanic fronts, which are sites of enhanced vertical motion, the metric performs worse than the other Eulerian metrics at identifying regions of strongest δz.

The benefit of using Lagrangian TZs is also observed for the larger scale models in Fig. 4d–i. For the 12 h analysis of the process study model, Fig. 4d demonstrates that the Lagrangian dilation rate TZs are more than twice as likely to predict regions with $\delta z = 4$ m compared to

the Eulerian divergence TZs, which is half the maximum value of δz for the model. The Lagrangian TZs are more likely to locate regions of large downward displacements, as indicated by Fig. 4e, and the median δz corresponding to Lagrangian TZs (~ 4 m) are four times the value of the Eulerian divergence TZs (~ 1 m). Lagrangian TZs rarely identify regions of upwelling in the process study model with $\bar{F}(\delta z = 0|\text{Target}) \sim 1$, as opposed to ~ 0.7 for the Eulerian ones. Finally, as presented in Fig. 4f, the Lagrangian TZs identify majority (dilation rate TZs identify 99.4%) of the regions of strongest downward vertical displacement where $\delta z > 6$ m (which constitute only 0.1% of the domain) while the Eulerian TZs continue to miss many of these regions, capturing less than 27%. Amongst the Eulerian metrics, the vertical velocity TZs perform better than the other Eulerian metrics in this model. This is because the vertical velocity was computed slightly below the ocean surface for numerical accuracy (discussed in the methods section). The effect of the small vertical displacement in the depth where $-w$ TZs are computed is magnified as a result of the relatively small amounts of δz in the process study model. It is important to remember, however, that obtaining accurate vertical velocities in the real ocean is difficult, and hence this curve should only be used as a barometer for the other metrics.

The strongest demonstration of the benefit of using Lagrangian TZs is in the most realistic setting, the data-assimilative real-time operational model of the western Mediterranean. For the 12 h analysis, the PDFs for Eulerian TZs (Fig. 4g) have a large peak near $\delta z = 0$, whereas the curves for Lagrangian TZs are flatter with a peak near 12 m. The median δz detected by the Lagrangian TZs (~ 12 m) is four times larger than the Eulerian TZ results (~ 3 m). As seen in Fig. 4h, Lagrangian TZs are more likely to predict large downward vertical displacement. For example, the Lagrangian TZs have a 30% chance to locate $\delta z \geq 20$ m as opposed to less than 10% for the Eulerian TZs. Not only are Lagrangian TZs more likely to locate large δz, they also locate a majority of the regions of strongest δz. Specifically, dilation rate TZs locate 91% of the regions where $\delta z > 40$ m despite this only occurring in 0.1% of the domain (Fig. 4i). In the case of the analysis of the operational model, the average mixed layer depth for the domain is approximately 10 m. This value is in agreement with the average mixed layer depth of this region reported in literature, which lies between 5 and 30 m in April (d'Ortenzio et al., 2005; Mason et al., 2019; Tarry et al.,
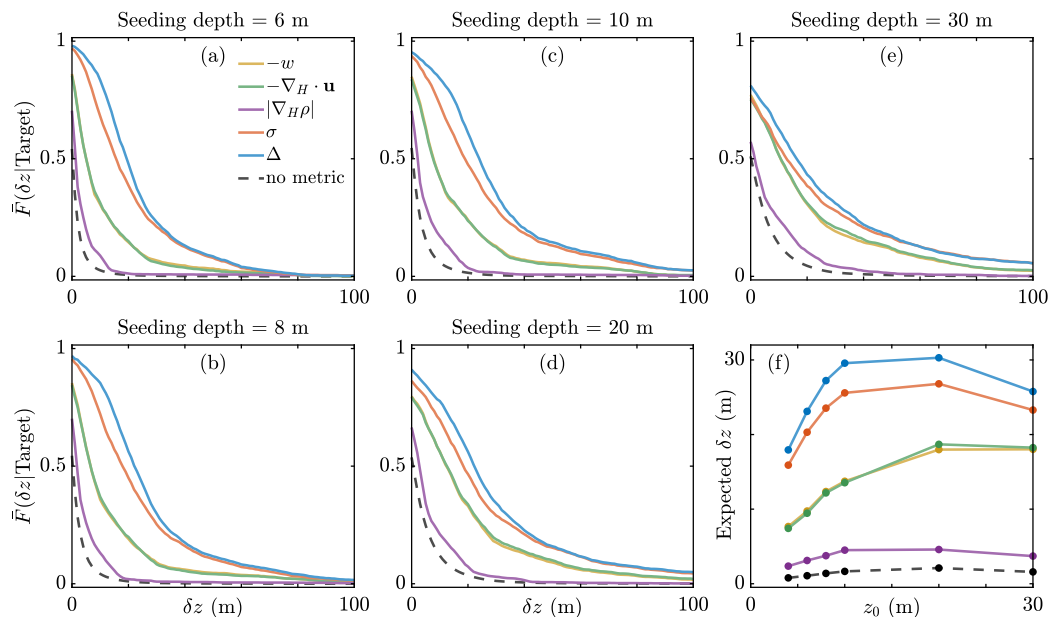
Fig. 5. Variation of skill with seeding depth. (a–e) Complementary cumulative distribution functions $\bar{F}(\delta z|\text{Target})$ for five different seeding depths at which particles are initialized to compute downward vertical displacement, plotted as a function of the resulting δz, for the operational model of the western Mediterranean. The target zones are computed using Lagrangian and Eulerian metrics computed on the ocean surface. (f) Expected δz for TZs of each metric, plotted as a function of the seeding depth, z_0. The curve for the no metric case (black dashed) has also been plotted for reference.

2021). This indicates that some of the identified regions are possibly experiencing subduction in our analysis of the operational model of the western Mediterranean.

3.3. Effect of varying the seeding depth

In the previous sections, Lagrangian metrics computed on the surface of the ocean were shown to better identify signatures of strong sub-surface δz compared to Eulerian metrics. The three dimensional trajectories used to compute δz for these analyses were initialized at a depth of 4 m, and it is worthwhile investigating how the results change when particles are seeded further below the surface. In this section, we investigate how the cumulative CDFs for the operational model change when the initialization depth is varied to understand how far below the surface the target zones are valid.

Fig. 5 presents the variation of the cumulative CDF for the five metrics (as well as the reference curve for the no metric case) for five different seeding depths: $z_0 = 6$, 8, 10, 20 and 30 m. In this figure, the δz axis has been extended to 100 m to accommodate the increased downward vertical displacement observed at deeper z_0. The cumulative CDFs for $z_0 \leq 10$ m are qualitatively similar, albeit with an increase in median δz for the dilation rate TZs to 24 m for $z_0 = 10$ m and a small decay in $\bar{F}(\delta z = 0|\text{Target})$. The latter suggests a growing frequency of incorrectly targeting regions with small amounts of upwelling. For deeper δz measurements, $\bar{F}(\delta z = 0|\text{Target})$ decays to 0.91 and 0.81 for $z_0 = 20$ m and 30 m, respectively, indicating a further increase in erroneously identifying upwelling regions as downwelling. For dilation rate TZs, the median δz for $z_0 = 20$ m and 30 m are also smaller at 22 m and 17 m, respectively, which means that the correlation between the surface signatures of the conduits, identified using the metrics, and their locations at deeper layers decay for $z_0 > 10$ m. This is because the vertical displacement conduits located near density fronts are not strictly vertical (i.e., they are located at an angle with the vertical that is dependent on the front angle), and as a result the boundaries of the conduits below the surface may be horizontally shifted from their surface signatures. For the two deepest z_0, the benefit of using Lagrangian metrics over Eulerian ones decreases, since the improvement is overshadowed by the decrease in correspondence between the surface and sub-surface. The median δz for the entire

domain (i.e., no metric case) increases, however, which suggests that even though the magnitude of vertical displacement increases, a decay in the correspondence between surface metrics and the sub-surface dynamics results in reduced benefit of using the surface TZs. While the benefit of using a Lagrangian target zone decays for deeper $z_0 = 30$ m, using a surface target zones (with the exception of the density gradient TZs) is still more beneficial than randomly sampling the domain. The variation with seeding depth z_0 in the skill associated with each metric is summarized using the expected δz for each target zone, presented in Fig. 5(f). The expected δz increases with seeding depth for all metrics until $z_0 = 10$ m, since the particles originate close enough to the surface to have strong correspondence to surface signatures, while being deep enough to displace further downward, faster. From $z_0 = 10$ m to 20 m, the expected δz remains nearly constant for the Lagrangian metrics σ and Δ, but not for $-w$ and $-\nabla_H \cdot \mathbf{u}$. This occurs despite the TZs locating conduits that displace water parcels deeper because the extent of non-downwelling regions located by the TZs increases with z_0 (as seen by the decrease in $\bar{F}(\delta z = 0|\text{Target})$) for σ and Δ, but remains nearly the same for $-w$ and $-\nabla_H \cdot \mathbf{u}$. Regardless, the magnitudes of expected δz for the Lagrangian TZs remain 50% more than the values for the two Eulerian TZs. The expected δz does not improve any further for $z_0 = 30$ m, even for $-w$ and $-\nabla_H \cdot \mathbf{u}$ TZs, because the correspondence between the surface and the sub-surface breaks down.

To better understand the weakening relationship between surface metrics and δz for particles starting deeper below the surface, we evaluate the correlation between two-dimensional trajectories that are artificially restricted to the ocean surface, like drifter data would be, and the three-dimensional trajectories of particles seeded at various depths. To evaluate this, we compute the horizontal separation, d_h, between the two-dimensional surface trajectories and the surface projections of the fully three-dimensional trajectories at the final instant of the 12 h advection interval as a function of the particles being inside or outside the dilation rate target zone.

Fig. 6 compares the statistics of d_h for particles seeded at the six different depths. The fraction of particles seeded inside (Fig. 6a) and outside (Fig. 6b) the dilation rate target zones that have horizontal separations $d_h < 1$ km, 1 km $< d_h < 5$ km, 5 km $< d_h < 10$ km and $d_h > 10$ km are presented for each z_0. For particles released nearest to the ocean surface, the majority of three dimensional trajectories remain
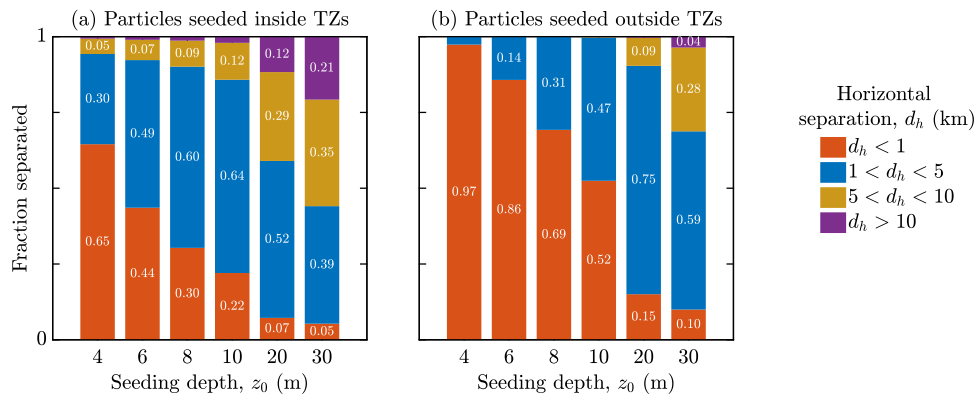
Fig. 6. Statistics of horizontal separation (d_h) between two-dimensional surface trajectories and the three-dimensional trajectories of particles seeded (a) inside and (b) outside the dilation rate target zones. The three dimensional trajectories are computed for particles seeded at six different depths: $z_0 = 4\,\text{m}$, $6\,\text{m}$, $8\,\text{m}$, $10\,\text{m}$, $20\,\text{m}$ and $30\,\text{m}$. The fraction of trajectories with $d_h < 1\,\text{km}$ (red bars), $1\,\text{km} < d_h < 5\,\text{km}$ (blue bars), $5\,\text{km} < d_h < 10\,\text{km}$ (yellow bars) and $d_h > 10\,\text{km}$ (purple bars) are presented for each z_0.

less than $1\,\text{km}$ away from the corresponding surface trajectory. There is a greater separation for particles that are released inside the TZs as 5% of trajectories have a final $d_h > 5\,\text{km}$. As particles are seeded deeper in the domain the similarity between the surface and three dimensional trajectory monotonically decreases. Despite this, the trend that trajectories outside the TZs are approximately twice as likely to remain less than $1\,\text{km}$ is consistent. For seeding depths up to $10\,\text{m}$, a negligible fraction of trajectories released outside the TZs have greater than $5\,\text{km}$ separation, which confirms that the vast majority of the upper ocean moves predominately in a two dimensional manner with the surface trajectories being well correlated with the horizontal projections of the fully three dimensional trajectories. Meanwhile greater than $5\,\text{km}$ separation is observed between 5 and 14% of the time within the dilation rate TZs, which correspond to sites of increased vertical displacement as discussed in the previous sections.

Even within the TZs, larger horizontal separation corresponds to greater δz. For particles seeded inside TZs at $z_0 = 4\,\text{m}$, the median δz corresponding to $d_h < 1\,\text{km}$ is only $12\,\text{m}$, but it increases to $23\,\text{m}$ for $1\,\text{km} < d_h < 5\,\text{km}$ and $25\,\text{m}$ for $5\,\text{km} < d_h < 10\,\text{km}$. The median δz for the trajectories that separate the most ($d_h > 10\,\text{km}$, which corresponds to only 0.7% of the target zones), however, is $53\,\text{m}$, confirming that the trajectories that are displaced downward the most correspond to the largest horizontal separation. Vertical displacement along the coherent conduits that have a preferred orientation likely plays a role here, since enhanced vertical velocity alone need not correspond to increased horizontal separation d_h. For a seeding depth of $z_0 = 10\,\text{m}$, 2% of particles seeded inside the TZs result in $d_h > 10\,\text{km}$, whereas only 0.3% of those seeded outside separate even $5\,\text{km}$. For the larger seeding depths of $20\,\text{m}$ and $30\,\text{m}$, a non-trivial fraction of trajectories initialized outside the dilation rate TZs obtained using surface metrics separate more that $5\,\text{km}$. These trajectories that separate the most are still linked to particles that are vertically displaced more than the average, but the horizontal shift in the location of the conduits at this depth compared to the surface results in the surface TZs not capturing some of the trajectories that are the displaced the most vertically.

### 3.4. Effect of varying the time intervals of analysis

We have shown for all three models that the Lagrangian TZs identify regions of high δz better than Eulerian TZs for a fixed time interval. The length of the time interval of analysis plays a significant role in both the δz and Lagrangian metric calculations, so it is worthwhile considering how the TZs perform for varying integration times and in cases where the Lagrangian metrics are calculated over a different time interval than the δz. For practical purposes, factors such as the frontal strength and eddy dynamics may affect the length of time over which subduction events occur. Hence, we consider a range of displacement times T_d

applied to the operational model of the western Mediterranean, for particles seeded at a depth of $4\,\text{m}$. Fig. 7a presents the effects of varying T_d, while maintaining $T_L = T_d$, on the median δz and the interquartile range for each of the five TZs. Note that varying T_L does not affect the Eulerian TZs since these metrics are computed only at the initial instant. The δz field, however, does vary with a change in T_d, and hence the median associated with Eulerian TZs will depend on T_d. As the length of the time interval increases, the median δz for the Lagrangian dilation rate TZs rapidly increases before peaking at $\sim 40\,\text{m}$ at $T_L = 30\,\text{h}$. The peak may indicate that there is a slowing of vertical displacement after $T_d = T_L \sim 40\,\text{h}$, or that there is a limit to the correspondence of the surface signatures to the dynamics well below the surface. The median δz from the Eulerian TZs also increases but is never more than $4\,\text{m}$, with the density gradient TZs yielding a lower median δz than the other two metrics. The difference between Lagrangian and Eulerian TZs is so significant that almost the entire interquartile range for the Lagrangian dilation rate TZs is always larger than the third quartile for the Eulerian TZs. For reference, the median δz and the interquartile range have also been plotted in black for the case without any target zone (i.e., sampling the entire domain). The median δz in this case is increasing but remains close to zero, indicating that despite extending the time interval considered there remains on average negligible net upward or downward motion associated with particles that start at a depth of $4\,\text{m}$.

From a practical perspective, experiments may need to be performed over displacement times longer than the time interval over which accurate model flow fields are available, since forecasts are less reliable further into the future. Hence, the efficacy of Lagrangian target zones computed over the time-scale of half a day for various displacement times is investigated. Fig. 7b highlights that, for a constant $T_L = 12\,\text{h}$, the Lagrangian TZs still achieve larger median δz and interquartile ranges than Eulerian ones for $T_d > 6\,\text{h}$. Comparing the median δz curves for the Lagrangian TZs when either $T_L = 12\,\text{h}$ or $T_L = T_d$, Fig. 7c demonstrates that although it is better to compute the Lagrangian TZs over the same time interval as δz a half-day computation yields median δz values of the same order of magnitude. When T_L is held constant, although there is a local maximum in median δz for the Lagrangian TZs around $T_d = 24\,\text{h}$ the median δz plateaus for longer T_d. For both studies, the Lagrangian TZs based on dilation rate consistently outperforms FTLE in identifying regions of high δz.

3.5. Ensemble analysis of the operational model

Another challenge for using Lagrangian target zones is that the true velocity field is not known beforehand and there are uncertainties associated with the ocean model fields as a result of parametrizations of unresolved processes and specifications of initial and boundary
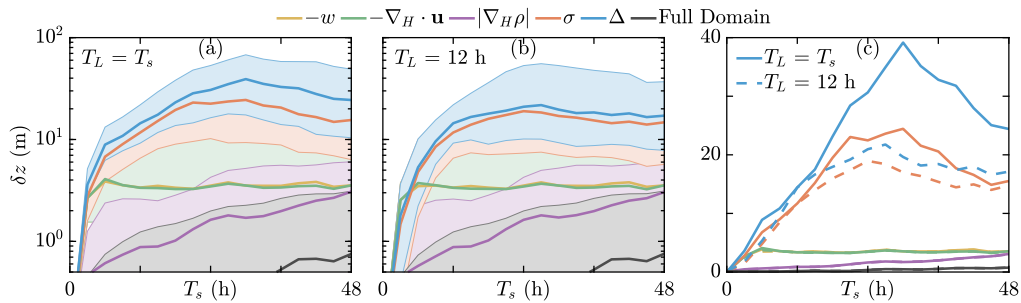
Fig. 7. Effect of analysis time intervals on median δz for the five target zones, applied to the operational model of the western Mediterranean. Median δz and interquartile ranges are plotted on a logarithmic-scale as a function of displacement time (T_d), with the time interval for Lagrangian target zone calculation (T_L) set to (a) the same value as T_d and (b) a value of 12 h. (c) Median δz curves (linear-scale) for target zones corresponding to the two Lagrangian metrics FTLE and dilation rate from (a) and (b) for comparison. The median δz for the entire domain (black) without any targeting remains close to zero over the 48 h interval, highlighting the importance of using efficient targeting methods.
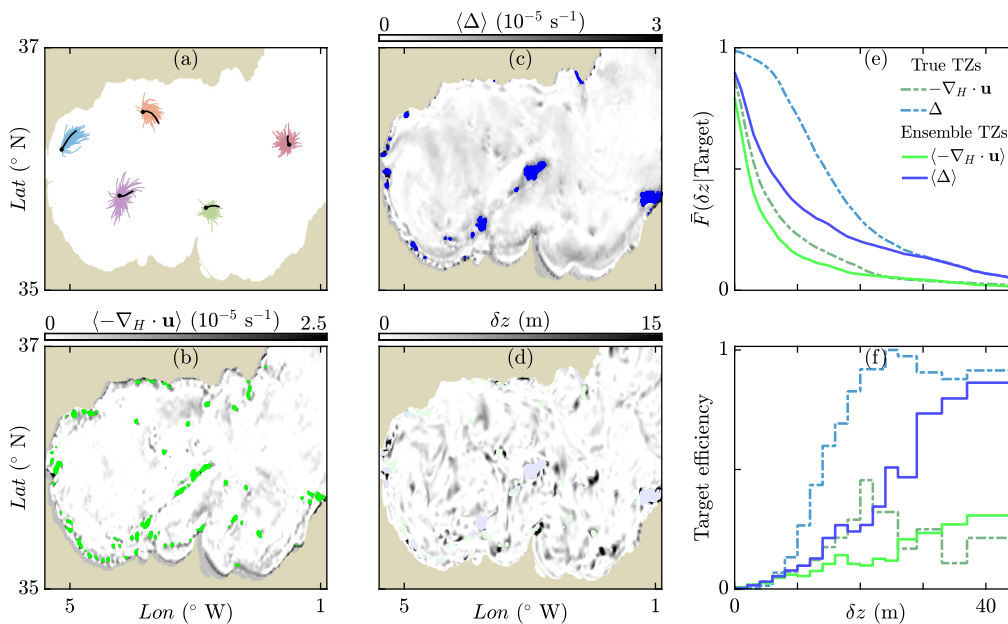
Fig. 8. Ensemble analysis of the operational model of the western Mediterranean. (a) Surface trajectories of particles released at five locations for 190 realizations (color); black lines correspond to trajectories from the "true" realization. Ensemble averaged (b) negative horizontal divergence, $-\nabla_H \cdot \mathbf{u}$, and (c) dilation rate, Δ, fields, with corresponding target zones overlaid. (d) Ensemble target zones obtained in (b) and (c) overlaid on the true δz field. (e) Complementary CDF of δz for the two ensemble-averaged (solid lines) and the true (dashed) target zones. (f) Target efficiency of high-δz regions in the true realization that are identified by the two ensemble (solid lines) and the true (dashed lines) target zones.

conditions (Lermusiaux et al., 2006a). To investigate the effectiveness of the TZs without knowledge of the actual velocity field, we perform an ensemble analysis of the western Mediterranean. Specifically, 191 realizations of real-time forecasts of the western Mediterranean were first generated using the Error Subspace Statistical Estimation schemes (Lermusiaux, 2002; Mahadevan et al., 2020b). One realization was then randomly chosen to be the "true" outcome, which was the realization presented in the previous sections, while the remaining 190 were used to compute the ensemble TZs. Similar results are obtained when selecting other realizations to be the "truth". The ensemble TZs for each metric are the regions with values in the ninety-ninth percentile of the ensemble averaged field, obtained by averaging the metric over the 190 realizations. The ensemble TZs were then compared to the high-δz regions in the true realization to evaluate the efficacy of each metric to be used in a predictive sense. For clarity, only the results for Eulerian divergence and the Lagrangian dilation rate are presented in this study. Results for the other metrics are presented in Figure S6 (Supporting Information).

Fig. 8a presents surface trajectories of particles seeded at five different locations for each of the 190 realizations, as well as the true realization. The high degree of variability in surface trajectories, as evidenced by relative dispersion of up to 40 km, reflects the variability in the ensemble velocity fields. The uncertainties were forecast to be large due to the limited observations available in real-time and the significant submesoscale variability. The accuracy of these real-time ensemble forecasts was validated using real drifter trajectories and other datasets (http://mseas.mit.edu/sea_exercises/CALYPSO/2019/). The divergence and dilation rate fields were computed for each realization over half a day (for this analysis, $T_d = T_L = 12$ h), and the ensemble average of these fields is presented in Fig. 8b,c. The TZs obtained from the ensemble-averaged fields are overlaid in black. The variability in the Eulerian metric has averaged out to give negligible values in the bulk of the Mediterranean in Fig. 8b, which results in the near-absence of Eulerian TZs away from the shore. For reference, the peak divergence value for the true realization is 0.33×10^{-3} s^{-1}, and the ensemble-average at that position is 0.2×10^{-4} s^{-1}. The resulting TZs in Fig. 8b are significantly different from the green regions for the TZs using the "true" velocity presented in Fig. 3e. The Lagrangian TZs are more robust to model uncertainties as the ensemble-averaged field in Fig. 8c yields well-defined TZs in the bulk of the Mediterranean that are reminiscent of the blue TZs in Fig. 3f. To elucidate, the overlap between ensemble TZs and true TZs for the Lagrangian metric dilation

rate is better with a 34% overlap, compared to a 16% overlap for the Eulerian metric divergence.

Fig. 8d presents the TZs from the ensemble-averaged fields overlaid on the δz field from the true realization. The dilation rate TZs align better with the high δz regions compared to the divergence TZs, demonstrating that the Lagrangian dilation rate captures regions of high downward vertical displacement better than its Eulerian counterpart, the divergence. This result is further demonstrated by $\bar{F}(\delta z|\text{Target})$ in Fig. 8e. Although the ensemble Lagrangian TZs perform better than the ensemble Eulerian TZs, a comparison with the true Lagrangian TZs reveals the cost of not having the true velocity field. Understandably, the ensemble Lagrangian TZs performs worse than the true Lagrangian TZs for $\delta z < 35$ m. What is remarkable, however, is that the ensemble-averaged Lagrangian TZs are almost as good as the true TZs for larger values of δz. This indicates that signatures of the strongest downwelling regions were captured by the Lagrangian TZs in most of the 190 realizations, as can be seen in Fig. 8f. The ensemble-averaged Lagrangian TZs are able to identify ∼50% of the regions of strongest δz, similar to the true Lagrangian TZs. Our result that target zones corresponding to the Lagrangian metric dilation rate is capable of detecting persistent regions of high δz is complementary to the result that Lagrangian coherent structure calculations using the Lagrangian metric FTLE is robust to model error (Haller, 2002; Lermusiaux and Lekien, 2005; Lermusiaux et al., 2006a). The ensemble-averaged and true Eulerian TZs are comparable for $\delta z > 30$ m, but fail to perform as well as the ensemble-averaged Lagrangian TZs for all values of δz. This means that the Lagrangian TZs computed without knowledge of the true fields can identify the true high-δz regions better than the Eulerian TZs computed using the true velocity fields. Therefore, if a realistic ensemble forecast is available, Lagrangian TZs based on this forecast can be used as predictors of regions of strong sub-surface downward vertical displacement more accurately than Eulerian TZs using the current velocity field.

4. Discussion

Vertical transport plays a crucial role in the dynamics of the upper ocean, and the use of Lagrangian surface target zones enhances the ability to locate conduits of downward displacement. We proposed the use of target zones (TZs) based on two Lagrangian metrics to identify regions of strong downward vertical displacement (δz), and compared them with three Eulerian metric TZs for a turbulence resolving model of a density front, a process study model of a density front, and a data-assimilative real-time operational model of the western Mediterranean. The five metrics were computed on the ocean surface with only surface fields, and the regions with values in the ninety-ninth percentile were chosen to be TZs for potential high-δz conduits. The performance of each TZ was evaluated by comparing their location with the δz field computed below the ocean surface. Although all five metrics highlighted regions of downward vertical displacement better than randomly sampling the domain, the Lagrangian TZs overlap better with regions of high δz. This resulted in Lagrangian TZs having a higher probability of predicting regions of high δz, regardless of the length scales in the model, and larger median δz. Lagrangian TZs outperformed Eulerian ones for the full range of time intervals analyzed, with median δz up to an order of magnitude larger for the operational model. Not only are the Lagrangian TZs more likely to identify regions of high δz, but they also identify a large fraction of the strongest δz regions. Almost half of the regions with strongest downward vertical displacement in the operational model align with the Lagrangian TZs, despite the target zones constituting only 1% of the entire domain.

Having demonstrated the consistent benefit of using Lagrangian TZs to identify regions of strong sub-surface vertical displacement, we considered two practical concerns of employing this method: (a) availability of forecast fields for displacement times of interest, and (b) sensitivity of results to model uncertainty. In practice, experiments

might need to be performed over displacement times longer than the time interval for which accurate forecast fields are available or target zone computation is reliable. Analysis of the operational model demonstrated that a 12-hour Lagrangian analysis is sufficient to predict high-δz regions for up to two days, with longer analysis only resulting in modest improvements. Since these methods may be used in a predictive sense, the actual velocity field may not be available for the Lagrangian analysis. The ensemble analysis of the western Mediterranean demonstrated that even when the true velocities are not known, and only an ensemble forecast is available, Lagrangian TZs are able to predict high-δz regions. Specifically, we demonstrated that Lagrangian TZs computed from an ensemble forecast fields perform nearly as well as the true Lagrangian TZs for regions with $\delta z > 35$ m. Interestingly, the ensemble Lagrangian TZs performed better than the true Eulerian TZs, indicating that a Lagrangian analysis of realistic forecasts is better at identifying the regions of strongest δz than Eulerian targeting based on the actual velocity fields.

The ability of Lagrangian metrics to predict high-δz regions is indicative of their link to vertical transport in the ocean, and opens up the possibility for more detailed studies of the phenomenon from a Lagrangian perspective. Our analysis has located strong vertical displacement exclusively using surface information. To identify where particles originally in the mixed layer are transported below it, accounting for the mixed layer depth in conjunction with the target zones may provide a means for differentiating between vertical displacement and subduction. There are potential benefits of considering combinations of the Lagrangian metrics and measurable ocean properties. For instance, the Lagrangian dilation rate TZs could be used in conjunction with the measured density gradient indicative of an oceanic density front to only target the vertical displacement regions associated with frontal submesoscale processes, in order to identify the coherent subduction conduits. A drifter release strategy leveraging the forecasted TZs and mixed layer depths could then be devised to more confidently identify surface signatures of subduction. Surface drifter trajectories, however, can differ based on the type of drifter due to buoyancy and windage effects (Olascoaga et al., 2020), and it remains to be determined how drifter convergence zones (Molinari and Kirwan, 1975; Berta et al., 2016) reflect the ocean surface TZs. Investigation of how TZs are modified by inertial effects when metrics like divergence and dilation rate are estimated using drifters will allow us to discard spurious surface signatures of convergence. These developments could potentially allow for direct identification of sites of strong vertical displacement and subduction based on forecasts and drifter based measurements, resulting in significant savings and a more efficient investigation of the ocean physics.

CRediT authorship contribution statement

H.M. Aravind: Data curation, Formal analysis, Investigation, Methodology, Software, Validation, Visualization, Writing – original draft, Writing – review & editing. **Vicky Verma:** Investigation, Writing – review & editing. **Sutanu Sarkar:** Funding acquisition, Investigation, Resources, Writing – review & editing. **Mara A. Freilich:** Investigation, Writing – review & editing. **Amala Mahadevan:** Funding acquisition, Investigation, Resources, Writing – review & editing. **Patrick J. Haley:** Investigation, Writing – review & editing. **Pierre F.J. Lermusiaux:** Funding acquisition, Investigation, Resources, Writing – review & editing. **Michael R. Allshouse:** Conceptualization, Funding acquisition, Investigation, Methodology, Project administration, Resources, Supervision, Writing — original draft, Writing – review & editing.

Declaration of competing interest

The authors declare that they have no known competing financial interests or personal relationships that could have appeared to influence the work reported in this paper.

Acknowledgments

Appendix A. Supplementary data

Supplementary material related to this article can be found online at https://doi.org/10.1016/j.ocemod.2022.102136.

References

Allshouse, M.R., Peacock, T., 2015. Lagrangian based methods for coherent structure detection. Chaos 25 (9), 097617. http://dx.doi.org/10.1063/1.4922968.

Barkan, R., Molemaker, M.J., Srinivasan, K., McWilliams, J.C., D'Asaro, E.A., 2019. The Role of Horizontal Divergence in Submesoscale Frontogenesis. J. Phys. Oceanogr. 49 (6), 1593–1618. http://dx.doi.org/10.1175/JPO-D-18-0162.1.

Berta, M., Griffa, A., Haza, A., Horstmann, J., Huntley, H., Ibrahim, R., Lund, B., Özgökmen, T., Poje, A., 2020. Submesoscale kinematic properties in summer and winter surface flows in the northern gulf of Mexico. J. Geophys. Res.: Oceans 125 (10), e2020JC016085. http://dx.doi.org/10.1029/2020JC016085.

Berta, M., Griffa, A., Özgökmen, T.M., Poje, A.C., 2016. Submesoscale evolution of surface drifter triads in the Gulf of Mexico. Geophys. Res. Lett. 43 (22), 11,751–11,759. http://dx.doi.org/10.1002/2016GL070357.

Choi, J., Bracco, A., Barkan, R., Shchepetkin, A.F., McWilliams, J.C., Molemaker, J.M., 2017. Submesoscale dynamics in the northern Gulf of Mexico. Part III: Lagrangian implications. J. Phys. Oceanogr. 47 (9), 2361–2376. http://dx.doi.org/10.1175/JPO-D-17-0036.1.

D'Asaro, E.A., Shcherbina, A.Y., Klymak, J.M., Molemaker, J., Novelli, G., Guigand, C.M., Haza, A.C., Haus, B.K., Ryan, E.H., Jacobs, G.A., Huntley, H.S., Laxague, N.J.M., Chen, S., Judt, F., McWilliams, J.C., Barkan, R., Kirwan, A.D., Poje, A.C., Özgökmen, T.M., 2018. Ocean convergence and the dispersion of flotsam. Proc. Natl. Acad. Sci. 115 (6), 1162–1167. http://dx.doi.org/10.1073/pnas.1718453115.

Denman, K., Gargett, A., 1995. Biological-physical interactions in the upper ocean: the role of vertical and small scale transport processes. Annu. Rev. Fluid Mech. 27 (1), 225–256. http://dx.doi.org/10.1146/annurev.fl.27.010195.001301.

Dever, M., Freilich, M., Cutolo, E., 2020. PSOM/V1.0: PSOM v1.0 - Freilich & Mahadevan. http://dx.doi.org/10.5281/zenodo.3902273.

d'Ortenzio, F., Iudicone, D., de Boyer Montégut, C., Testor, P., Antoine, D., Marullo, S., Santoleri, R., Madec, G., 2005. Seasonal variability of the mixed layer depth in the Mediterranean Sea as derived from in situ profiles. Geophys. Res. Lett. 32 (12), http://dx.doi.org/10.1029/2005GL022463.

d'Ovidio, F., Isern-Fontanet, J., López, C., Hernández-García, E., García-Ladona, E., 2009. Comparison between Eulerian diagnostics and finite-size Lyapunov exponents computed from altimetry in the Algerian basin. Deep Sea Res. Part I 56 (1), 15–31. http://dx.doi.org/10.1016/j.dsr.2008.07.014.

Dusenberry, J.A., Olson, R.J., Chisholm, S.W., 1999. Frequency distributions of phytoplankton single-cell fluorescence and vertical mixing in the surface ocean. Limnol. Oceanogr. 44 (2), 431–435. http://dx.doi.org/10.4319/lo.1999.44.2.0431.

Egbert, G.D., Erofeeva, S.Y., 2002. Efficient inverse modeling of barotropic ocean tides. J. Atmos. Ocean. Technol. 19 (2), 183–204. http://dx.doi.org/10.1175/1520-0426(2002)019<0183:EIMOBO>2.0.CO;2.

Fischer, J., Visbeck, M., 1993. Deep Velocity Profiling with Self-contained ADCPs. J. Atmos. Ocean. Technol. 10 (5), 764–773. http://dx.doi.org/10.1175/1520-0426(1993)010<0764:DVPWSC>2.0.CO;2.

Freilich, M.A., Mahadevan, A., 2019. Decomposition of vertical velocity for nutrient transport in the upper ocean. J. Phys. Oceanogr. 49 (6), 1561–1575. http://dx.doi.org/10.1175/JPO-D-19-0002.1.

Freilich, M., Mahadevan, A., 2021. Coherent pathways for subduction from the surface mixed layer at ocean fronts. J. Geophys. Res.: Oceans 126 (5), e2020JC017042. http://dx.doi.org/10.1029/2020JC017042.

Giordani, H., Prieur, L., Caniaux, G., 2006. Advanced insights into sources of vertical velocity in the ocean. Ocean Dyn. 56, 513–524. http://dx.doi.org/10.1007/s10236-005-0050-1.

Gnanadesikan, A., Slater, R.D., Swathi, P.S., Vallis, G.K., 2005. The Energetics of Ocean Heat Transport. J. Clim. 18 (14), 2604–2616. http://dx.doi.org/10.1175/JCLI3436.1.

González-Gaya, B., Casal, P., Jurado, E., Dachs, J., Jiménez, B., 2019. Vertical transport and sinks of perfluoroalkyl substances in the global open ocean. Environ. Sci.: Proc. Impacts 21 (11), 1957–1969. http://dx.doi.org/10.1039/C9EM00266A.

Haley, P.J., Agarwal, A., Lermusiaux, P.F., 2015. Optimizing velocities and transports for complex coastal regions and archipelagos. Ocean Model. 89, 1–28. http://dx.doi.org/10.1016/j.ocemod.2015.02.005.

Haley, P.J., Lermusiaux, P.F.J., 2010. Multiscale two-way embedding schemes for free-surface primitive equations in the "Multidisciplinary Simulation, Estimation and Assimilation System". Ocean Dyn. 60 (6), 1497–1537. http://dx.doi.org/10.1007/s10236-010-0349-4.

Haller, G., 2001. Distinguished material surfaces and coherent structures in three-dimensional fluid flows. Physica D 149 (4), 248–277. http://dx.doi.org/10.1016/S0167-2789(00)00199-8.

Haller, G., 2002. Lagrangian coherent structures from approximate velocity data. Phys. Fluids A 14, 1851–1861. http://dx.doi.org/10.1063/1.1477449.

Haller, G., 2015. Lagrangian coherent structures. Annu. Rev. Fluid Mech. 47 (1), 137–162. http://dx.doi.org/10.1146/annurev-fluid-010313-141322.

Heburn, G.W., La Violette, P.E., 1990. Variations in the structure of the anticyclonic gyres found in the Alboran Sea. J. Geophys. Res.: Oceans 95 (C2), 1599–1613. http://dx.doi.org/10.1029/JC095iC02p01599.

Hernández-Carrasco, I., Orfila, A., Rossi, V., Garçon, V., 2018. Effect of small scale transport processes on phytoplankton distribution in coastal seas. Sci. Rep. 8 (1), 8613. http://dx.doi.org/10.1038/s41598-018-26857-9.

Huntley, H.S., Lipphardt Jr., B.L., Jacobs, G., Kirwan Jr., A.D., 2015. Clusters, deformation, and dilation: Diagnostics for material accumulation regions. J. Geophys. Res.: Oceans 120 (10), 6622–6636. http://dx.doi.org/10.1002/2015JC011036.

Lermusiaux, P.F.J., 2002. On the mapping of multivariate geophysical fields: Sensitivities to size, scales, and dynamics. J. Atmos. Ocean. Technol. 19 (10), 1602–1637. http://dx.doi.org/10.1175/1520-0426(2002)019<1602:OTMOMG>2.0.CO;2.

Lermusiaux, P.F., Chiu, C.-S., Gawarkiewicz, G.G., Abbot, P., Robinson, A.R., Miller, R.N., Haley, P.J., Leslie, W.G., Majumdar, S.J., Pang, A., et al., 2006a. Quantifying uncertainties in ocean predictions. Oceanography 19, 92–105.

Lermusiaux, P., Lekien, F., 2005. Dynamics and Lagrangian coherent structures in the ocean and their uncertainty. In: Extended Abstract in Report of the Dynamical System Methods in Fluid Dynamics Oberwolfach Workshop. Mathematisches Forschungsinstitut Oberwolfach, p. 2.

Lermusiaux, P.F., Malanotte-Rizzoli, P., Stammer, D., Carton, J., Cummings, J., Moore, A.M., 2006b. Progress and Prospects of US Data Assimilation in Ocean Research. Technical Report, Harvard univ cambridge ma.

Mahadevan, A., 2006. Modeling vertical motion at ocean fronts: Are nonhydrostatic effects relevant at submesoscales? Ocean Model. 14 (3), 222–240. http://dx.doi.org/10.1016/j.ocemod.2006.05.005.

Mahadevan, A., 2016. The impact of submesoscale physics on primary productivity of plankton. Annu. Rev. Mar. Sci. 8 (1), 161–184. http://dx.doi.org/10.1146/annurev-marine-010814-015912.

Mahadevan, A., D'Asaro, E.A., Allen, J.T., Almaraz García, P., Alou-Font, E., Aravind, H.M., Balaguer, P., Caballero, I., Calafat, N., Carbornero, A., Casas, B., Castilla, C., Centurioni, L.R., Conley, M., Cristofano, G., Cutolo, E., Dever, M., Enrique Navarro, A., Falcieri, F., Freilich, M., Goodwin, E., Graham, R., Guigand, C., Hodges, B.A., Huntley, H., Johnston, S., Lankhorst, M., Lermusiaux, P.F.J., Lizaran, I., Mirabito, C., Miralles, A., Mourre, B., Navarro, G., Ohmart, M., Ouala, S., Ozgokmen, T.M., Pascual, A., Pou, J.M.H., Poulain, P.M., Ren, A., Rodriguez Tarry, D., Rudnick, D.L., Rubio, M., Ruiz, S., Rypina, I.I., Tintore, J., Send, U., Shcherbina, A.Y., Torner, M., Salvador-Vieira, G., Wirth, N., Zarokanellos, N., 2020a. CALYPSO 2019 Cruise Report: field campaign in the Mediterranean. Technical Report, Woods Hole Oceanographic Institution, http://dx.doi.org/10.1575/1912/25266.

Mahadevan, A., Oliger, J., Street, R., 1996a. A nonhydrostatic mesoscale ocean model. Part I: Well-posedness and scaling. J. Phys. Oceanogr. 26 (9), 1868–1880. http://dx.doi.org/10.1175/1520-0485(1996)026<1868:ANMOMP>2.0.CO;2.

Mahadevan, A., Oliger, J., Street, R., 1996b. A nonhydrostatic mesoscale ocean model. Part II: Numerical implementation. J. Phys. Oceanogr. 26 (9), 1881–1900. http://dx.doi.org/10.1175/1520-0485(1996)026<1881:ANMOMP>2.0.CO;2.

Mahadevan, A., Pascual, A., Rudnick, D.L., Ruiz, S., Tintoré, J., D'Asaro, E., 2020b. Coherent pathways for vertical transport from the surface ocean to interior. Bull. Am. Meteorol. Soc. 1–21. http://dx.doi.org/10.1175/BAMS-D-19-0305.1.

Mahadevan, A., Tandon, A., 2006. An analysis of mechanisms for submesoscale vertical motion at ocean fronts. Ocean Model. 14 (3), 241–256. http://dx.doi.org/10.1016/j.ocemod.2006.05.006.

Marshall, D., 1997. Subduction of water masses in an eddying ocean. J. Mar. Res. 55 (2), 201–222. http://dx.doi.org/10.1357/0022240973224373.

Marshall, J.C., Williams, R.G., Nurser, A.G., 1993. Inferring the subduction rate and period over the North Atlantic. J. Phys. Oceanogr. 23 (7), 1315–1329. http://dx.doi.org/10.1175/1520-0485(1993)023<1315:ITSRAP>2.0.CO;2.

Martin, A.P., Richards, K.J., 2001. Mechanisms for vertical nutrient transport within a North Atlantic mesoscale eddy. Deep Sea Res. Part II 48 (4), 757–773. http://dx.doi.org/10.1016/S0967-0645(00)00096-5.

Mason, E., Ruiz, S., Bourdalle-Badie, R., Reffray, G., García-Sotillo, M., Pascual, A., 2019. New insight into 3-D mesoscale eddy properties from CMEMS operational models in the western mediterranean. Ocean Sci. 15 (4), 1111–1131. http://dx.doi.org/10.5194/os-15-1111-2019.

McWilliams, J.C., 2007. Irreducible imprecision in atmospheric and oceanic simulations. Proc. Natl. Acad. Sci. 104 (21), 8709–8713. http://dx.doi.org/10.1073/pnas.0702971104.

McWilliams, J.C., 2016. Submesoscale currents in the ocean. Proc. R. Soc. A 472 (2189), 20160117. http://dx.doi.org/10.1098/rspa.2016.0117.

Molinari, R., Kirwan, J., 1975. Calculations of Differential Kinematic Properties from Lagrangian Observations in the Western Caribbean Sea. J. Phys. Oceanogr. 5 (3), 483–491. http://dx.doi.org/10.1175/1520-0485(1975)005<0483:CODKPF>2.0.CO;2.

Nagai, T., Gruber, N., Frenzel, H., Lachkar, Z., McWilliams, J.C., Plattner, G.-K., 2015. Dominant role of eddies and filaments in the offshore transport of carbon and nutrients in the California Current System. J. Geophys. Res.: Oceans 120 (8), 5318–5341. http://dx.doi.org/10.1002/2015JC010889.

Nolan, P.J., Serra, M., Ross, S.D., 2020. Finite-time Lyapunov exponents in the instantaneous limit and material transport. Nonlinear Dynam. 100 (4), 3825–3852. http://dx.doi.org/10.1007/s11071-020-05713-4.

Olascoaga, M.J., Beron-Vera, F.J., Miron, P., Triñanes, J., Putman, N.F., Lumpkin, R., Goni, G.J., 2020. Observation and quantification of inertial effects on the drift of floating objects at the ocean surface. Phys. Fluids 32 (2), 026601. http://dx.doi.org/10.1063/1.5139045.

Olascoaga, M.J., Rypina, I.I., Brown, M.G., Beron-Vera, F.J., Koçak, H., Brand, L.E., Halliwell, G.R., Shay, L.K., 2006. Persistent transport barrier on the West Florida Shelf. Geophys. Res. Lett. 33 (22), http://dx.doi.org/10.1029/2006GL027800.

Omand, M.M., D'Asaro, E.A., Lee, C.M., Perry, M.J., Briggs, N., Cetinić, I., Mahadevan, A., 2015. Eddy-driven subduction exports particulate organic carbon from the spring bloom. Science 348 (6231), 222–225. http://dx.doi.org/10.1126/science.1260062.

Pascual, A., Ruiz, S., Olita, A., Troupin, C., Claret, M., Casas, B., Mourre, B., Poulain, P.-M., Tovar-Sanchez, A., Capet, A., Mason, E., Allen, J.T., Mahadevan, A., Tintoré, J., 2017. A multiplatform experiment to unravel meso- and submesoscale processes in an intense front (alborex). Fronti. Mar. Sci. 4, 39. http://dx.doi.org/10.3389/fmars.2017.00039.

Qu, T., Chen, J., 2009. A North Pacific decadal variability in subduction rate. Geophys. Res. Lett. 36 (22), http://dx.doi.org/10.1029/2009GL040914.

Reisser, J., Slat, B., Noble, K., Du Plessis, K., Epp, M., Proietti, M., De Sonneville, J., Becker, T., Pattiaratchi, C., 2015. The vertical distribution of buoyant plastics at sea: an observational study in the North Atlantic Gyre. Biogeosciences 12 (4), 1249–1256. http://dx.doi.org/10.5194/bg-12-1249-2015.

Rudnick, D.L., Klinke, J., 2007. The Underway Conductivity–Temperature–Depth Instrument. J. Atmos. Ocean. Technol. 24 (11), 1910–1923. http://dx.doi.org/10.1175/JTECH2100.1.

Ruiz, S., Claret, M., Pascual, A., Olita, A., Troupin, C., Capet, A., Tovar-Sánchez, A., Allen, J., Poulain, P.-M., Tintoré, J., Mahadevan, A., 2019. Effects of oceanic mesoscale and submesoscale frontal processes on the vertical transport of phytoplankton. J. Geophys. Res.: Oceans 124 (8), 5999–6014. http://dx.doi.org/10.1029/2019JC015034.

Serra, M., Haller, G., 2016. Objective Eulerian coherent structures. Chaos 26 (5), 053110. http://dx.doi.org/10.1063/1.4951720.

Siegelman, L., Klein, P., Rivière, P., Thompson, A.F., Torres, H.S., Flexas, M., Menemenlis, D., 2020. Enhanced upward heat transport at deep submesoscale ocean fronts. Nat. Geosci. 13 (1), 50–55. http://dx.doi.org/10.1038/s41561-019-0489-1.

Spall, M.A., 1995. Frontogenesis, subduction, and cross-front exchange at upper ocean fronts. J. Geophys. Res.: Oceans 100 (C2), 2543–2557. http://dx.doi.org/10.1029/94JC02860.

Sulman, M.H., Huntley, H.S., Lipphardt, B., Kirwan, A., 2013. Leaving flatland: Diagnostics for Lagrangian coherent structures in three-dimensional flows. Physica D 258, 77–92. http://dx.doi.org/10.1016/j.physd.2013.05.005.

Tanabe, S., Tatsukawa, R., 1983. Vertical transport and residence time of chlorinated hydrocarbons in the open ocean water column. J. Oceanogr. Soc. Jpn. 39 (2), 53–62. http://dx.doi.org/10.1007/BF02210759.

Tarry, D.R., Essink, S., Pascual, A., Ruiz, S., Poulain, P.-M., Özgökmen, T., Centurioni, L.R., Farrar, J.T., Shcherbina, A., Mahadevan, A., et al., 2021. Frontal convergence and vertical velocity measured by drifters in the alboran sea. J. Geophys. Res.: Oceans 126 (4), e2020JC016614. http://dx.doi.org/10.1029/2020JC016614.

Thomas, L.N., Tandon, A., Mahadevan, A., 2008. Submesoscale processes and dynamics. In: Ocean Modeling in an Eddying Regime. American Geophysical Union (AGU), pp. 17–38. http://dx.doi.org/10.1029/177GM04.

Tozer, B., Sandwell, D.T., Smith, W.H.F., Olson, C., Beale, J.R., Wessel, P., 2019. Global bathymetry and topography at 15 arc sec: SRTM15+. Earth Space Sci. 6 (10), 1847–1864. http://dx.doi.org/10.1029/2019EA000658.

Ullman, D.S., Hebert, D., 2014. Processing of Underway CTD Data. J. Atmos. Ocean. Technol. 31 (4), 984–998. http://dx.doi.org/10.1175/JTECH-D-13-00200.1.

Van Sebille, E., Griffies, S.M., Abernathey, R., Adams, T.P., Berloff, P., Biastoch, A., Blanke, B., Chassignet, E.P., Cheng, Y., Cotter, C.J., et al., 2018. Lagrangian ocean analysis: Fundamentals and practices. Ocean Model. 121, 49–75. http://dx.doi.org/10.1016/j.ocemod.2017.11.008.

Vargas-Yáñez, M., Plaza, F., Garcıa-Lafuente, J., Sarhan, T., Vargas, J., Vélez-Belchi, P., 2002. About the seasonal variability of the Alboran Sea circulation. J. Mar. Syst. 35 (3–4), 229–248. http://dx.doi.org/10.1016/S0924-7963(02)00128-8.

Verma, V., Pham, H.T., Sarkar, S., 2019. The submesoscale, the finescale and their interaction at a mixed layer front. Ocean Model. 140, 101400. http://dx.doi.org/10.1016/j.ocemod.2019.05.004.

Verma, V., Sarkar, S., 2021. Lagrangian three-dimensional transport and dispersion by submesoscale currents at an upper-ocean front. Ocean Model. 165, 101844. http://dx.doi.org/10.1016/j.ocemod.2021.101844.

Williams, R.G., Meijers, A., 2019. Ocean subduction. In: Cochran, J.K., Bokuniewicz, H.J., Yager, P.L. (Eds.), Encyclopedia of Ocean Sciences, 3rd ed. Academic Press, Cambridge, Massachusetts, United States, pp. 141–157. http://dx.doi.org/10.1016/B978-0-12-409548-9.11297-7.

Wunsch, C., Ferrari, R., 2004. Vertical mixing, energy, and the general circulation of the oceans. Annu. Rev. Fluid Mech. 36 (1), 281–314. http://dx.doi.org/10.1146/annurev.fluid.36.050802.122121.